

GHz dynamic holographic VCSEL chip via current-addressed modes multiplexing

Received: 4 May 2025

Accepted: 21 January 2026

Published online: 29 January 2026

 Check for updates

Xiaonan Hu^{1,2,4}, Yibo Dong^{1,2,4}, Jianyang Shi³, Baoli Li^{1,2}, Haitao Luan^{1,2},
Nan Chi³, Min Gu^{1,2}✉ & Xinyuan Fang^{1,2}✉

The intuitive wisdom in semiconductor laser engineering dictates that high-order spatial modes of vertical-cavity surface-emitting lasers (VCSELs) must be suppressed to preserve beam quality, despite their inherent potential as independent information carriers. Here, we develop current-addressed modes multiplexing holography in multimode VCSELs, where injection current-dependent dominant orbital angular momentum (OAM) components enhance information channel capacity and enable dynamic reconfigurability of holographic systems. Crucially, monolithic integration of laser-nanoprinted multiplexed holograms with VCSEL chips resolves the persistent contradiction between dynamic light-field manipulation and miniaturization of holographic optoelectronic systems. Experimental validation shows that a 2×2 chip array (unit area: ~100×100 μm²) enables dynamic 3D display with an ultrahigh refresh rate of ~1.93 GHz. To our knowledge, this represents the fastest holographic switching speed and most compact chip-scale system reported to date. This work establishes a platform for portable and wearable devices, ultrahigh-speed short-reach interconnects, virtual and augmented reality systems with minimized latency.

Holography provides an approach to record and reconstruct three-dimensional (3D) wavefronts of objects¹, which can be implemented in various fields, including displays, imaging², data storage³, optical communications⁴, information encryption⁵, and neuromorphic photonic computing⁶. To facilitate the practicality and adaptability of these applications in chip-scale, recent advancements have focused on miniaturization and dynamic switching capability of holographic systems^{7,8}. Spatial light modulators (SLMs) and digital micromirror devices (DMDs), combined with external laser sources, have been traditionally employed for dynamic wavefront manipulation. Nonetheless, both the complex addressing circuits embedded in these digital holographic devices and the bulky size of lasers impose fundamental challenges to achieve on-chip integration. This hinders the development of emerging wearable and portable holographic information processing products.

To address this problem, incorporating integrated light sources with diffractive optical elements (DOEs) has been proven as a promising compact and versatile photonic systems⁹. In this context, vertical-cavity surface-emitting lasers (VCSELs) have attracted tremendous attention^{10–12}. Such semiconductor lasers, with an epitaxial active layer and distributed Bragg reflectors (DBRs) to form the laser gain medium and resonant cavity, feature unique advantages including micron-scale size, two-dimensional (2D) array format, planar emitting surface, and high modulation speeds (above GHz). By further leveraging advanced micro- and nano-fabrication techniques (such as electron beam lithography and 3D laser nano-printing), optically digitalized holograms¹³ can be directly integrated onto the emitting surface of VCSELs to modulate the wavefront and the polarization states of output beams^{14–17}, which can significantly reduce the size of holographic systems. Unfortunately, as the overall area of hologram is

¹School of Artificial Intelligence Science and Technology, University of Shanghai for Science and Technology, Shanghai, China. ²Institute of Photonic Chips, University of Shanghai for Science and Technology, Shanghai, China. ³Key Laboratory for Information Science of Electromagnetic Waves (MoE), School of Information Science and Technology, Fudan University, Shanghai, China. ⁴These authors contributed equally: Xiaonan Hu, Yibo Dong.

✉ e-mail: gumin@usst.edu.cn; xinyuan.fang@usst.edu.cn

limited by the small emitting surface of VCSELs, the sub-micro- or nano-scale pixel resolution hinders the layout of addressing circuits to obtain an optoelectronic device for dynamic light-field control.

Other pioneering methods to dynamically manipulate the optically digitalized holograms have also been proposed, such as chemical reactions¹⁸, optical erasure and rewriting¹⁹, mechanical stretching²⁰, twisting cascaded holograms²¹, and thermal regulation²². Nevertheless, additional components or steps often slow down the switching frame rate and increase system complexity, which makes them inapplicable for VCSEL-integrated systems. Recently, the physical dimensions of light, such as wavelength²³, polarization²⁴, space²⁵, time²⁶, and modes²⁷, have been utilized to increase the information channels of optically multiplexed holograms. To be specific, optically addressable dynamic holography can be realized by selectively controlling the properties of the input and output beams²⁸. Therein, spatial modes multiplexing is particularly promising in boosting information channel capacity due to

its theoretically infinite states. Notably, since the transverse dimension of the active region is much larger than its longitudinal length, multi-mode VCSELs usually operate in multiple transverse spatial modes, which can even be switched by adjusting the injection current²⁹. As such, we exploit this fact to encode various holographic information channels into distinct transverse spatial modes from a multi-mode VCSEL and multiplex them into an optically digitalized hologram. Consequently, dynamic holography can be achieved by elaborately manipulating the injection current-dependent spatial modes.

Here, we develop a dynamic holographic VCSEL chip by integrating a multi-mode VCSEL with a current-addressed mode-multiplexed optically digitalized hologram. The principle to design such an ultra-compact holographic system with ultra-high switching frame rate is illustrated in Fig. 1. The lack of precise physical models of the output electrical fields from multi-mode VCSELs render it difficult to design the spatial mode-multiplexed hologram. To overcome this challenge,

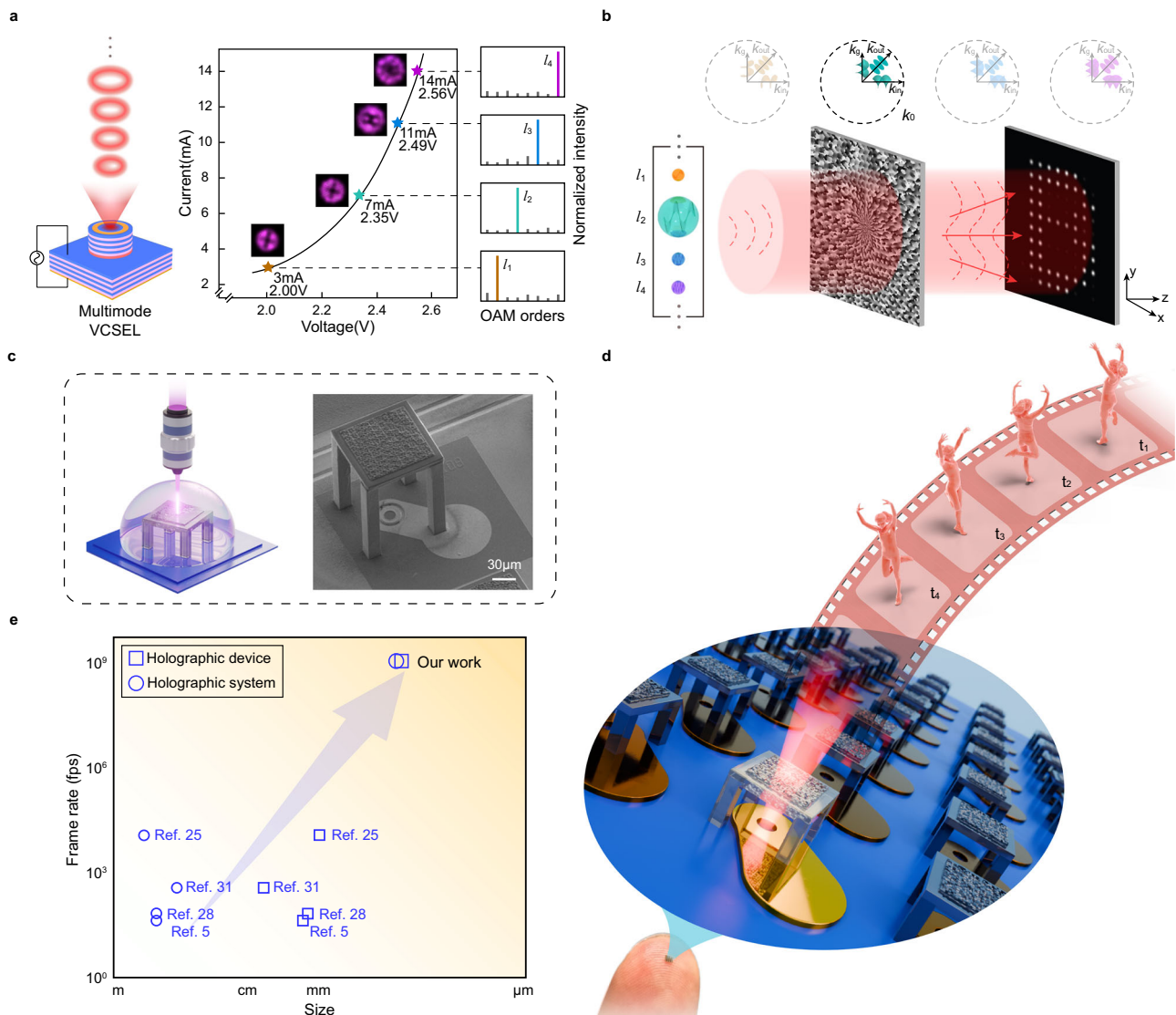


Fig. 1 | Schematic diagrams of structure, design principle and performances of the holographic VCSEL chip. a The injection current-dependent OAM modes weighting coefficient spectra of the multimode VCSEL. Four dominant OAM mode components at distinct currents (right panel) have been selected to design the OAM-multiplexing hologram. **b** Schematic of the selective holographic reconstruction of the OAM-multiplexing hologram using the multi-mode VCSEL at a specific injection current (7 mA). The big green circle in the left square bracket and the k-space analysis with solid lines (upper panel) reveal the largest OAM weighting

coefficient at l_2 . **c** Illustration of incorporating an optically digital hologram onto the VCSEL's surface through 3D laser nanoprining (left panel) and the scanning electron microscope (SEM) image of the holographic system (right panel). **d** The conceptual illustration of ultra-compact holographic VCSEL chip for 3D dynamic holographic display. **e** The comparison of our work with the state of the art. Here, the holographic system includes the laser source and the holographic device, which is related to the hologram.

the orthogonal orbital angular momentum (OAM) states have been utilized to encode holographic images³⁰ owing to the well-defined injection current-dependent OAM modes weighting coefficient spectrum (Fig. 1a). To minimize the channel crosstalk in optical multiplexed holography, the dominant OAM mode components characterized by the largest weighting coefficients (l_1, l_2, l_3 and l_4 in Fig. 1a) are selected in the design of the OAM-multiplexing hologram. In this regard, only a spatial mode state with a dominant OAM component (e.g., l_2 in Fig. 1b), given by the multi-mode VCSEL at a specific injection current, selectively reconstructs the target holographic image with a stronger Gaussian intensity profile at each pixel. Notably, the hologram can be directly integrated onto the VCSELs' surface using 3D laser nano-printing (Fig. 1c), which further enables a holographic VCSEL chip comprising hologram arrays (Fig. 1d). As such, a dynamic holographic display can be achieved by varying the injected currents of each device over time sequences. Compared with other schemes^{5,25,28,31}, our strategy illustrates a compact, all-in-one holographic system (including laser source and holographic devices) with only hundreds of microns. Moreover, the high-speed modulation capabilities of VCSELs allow theoretical frame rates exceeding 10^9 frames per second (Fig. 1e).

Results

OAM mode dynamics in multimode VCSELs

The physical mechanism of injection current-dependent OAM modes weighting coefficient spectra dynamics in multimode VCSELs is revealed in Fig. 2. Here, we explore the OAM mode components of VCSEL beams using the fiber model. Throughout this manuscript, oxidation-confined, top-emitting VCSELs emitting at ~905 nm have been employed, whose epitaxial structure mainly includes p-DBR, active region, n-DBR, and GaAs substrate (Fig. 2a). The fundamental properties of these VCSELs, including their spectral characteristics, I-V behavior, and lifetime, are presented in Supplementary Fig. 1–3 (“Methods”), respectively. In this context, the oxide aperture diameter

(d) denotes the unoxidized region in the oxidized layer. The refractive index (n_2) of the oxidized region is lower than that of the unoxidized region (n_1), forming a cylindrical waveguide structure. In this model, the unoxidized central current aperture serves as the waveguide core, while the oxide confinement layer acts as the cladding. By computing the refractive indices across all epitaxial layers, an average cladding-core index difference of approximately 0.01 can be obtained^{32,33}. As a result, using the weak-guidance approximation, a specific OAM mode state in VCSELs can be investigated by combining degenerate odd and even LP_{lm} modes with phase differences of $\pi/2$ or $3\pi/2$ (i.e., $OAM_{\pm l} = LP_{lma} \pm i \times LP_{lmb}$)³⁴. Here, l and m denote the azimuthal (OAM order) and radial indices, while a and b indicate the degenerate odd and even LP_{lm} modes, respectively. Notably, only the LP_{lm} modes with $m=1$ are considered owing to the degradation of higher-order LP modes in propagation. Next, represented by the LP modes with the same OAM mode order l , the OAM modes capacity of multi-mode VCSELs with different oxide aperture sizes have been analyzed in detail. For this purpose, the normalized frequency (V) determined by the oxide aperture diameter (d) in VCSELs has been calculated, which indicates the number of guided wave modes supported in such fiber model (Supplementary Note 1). Moreover, to figure out each particular guided LP modes, the longitudinal normalized propagation constant (β) representing the axial component of the light wave vector are constrained to be positive. As such, the VCSELs with larger oxide aperture sizes can support more OAM modes (Fig. 2b), laying the physical foundation for providing potential information channels in OAM multiplexing.

To further explore the injection current-dependent OAM modes competitions in multi-mode VCSELs, current density spatial distributions in the active layer and the resultant OAM modes components at various injection currents have been both studied based on the epitaxial structure and doping concentration (Supplementary Table 1). As shown in Fig. 2c, while the charge carrier distribution exhibits a

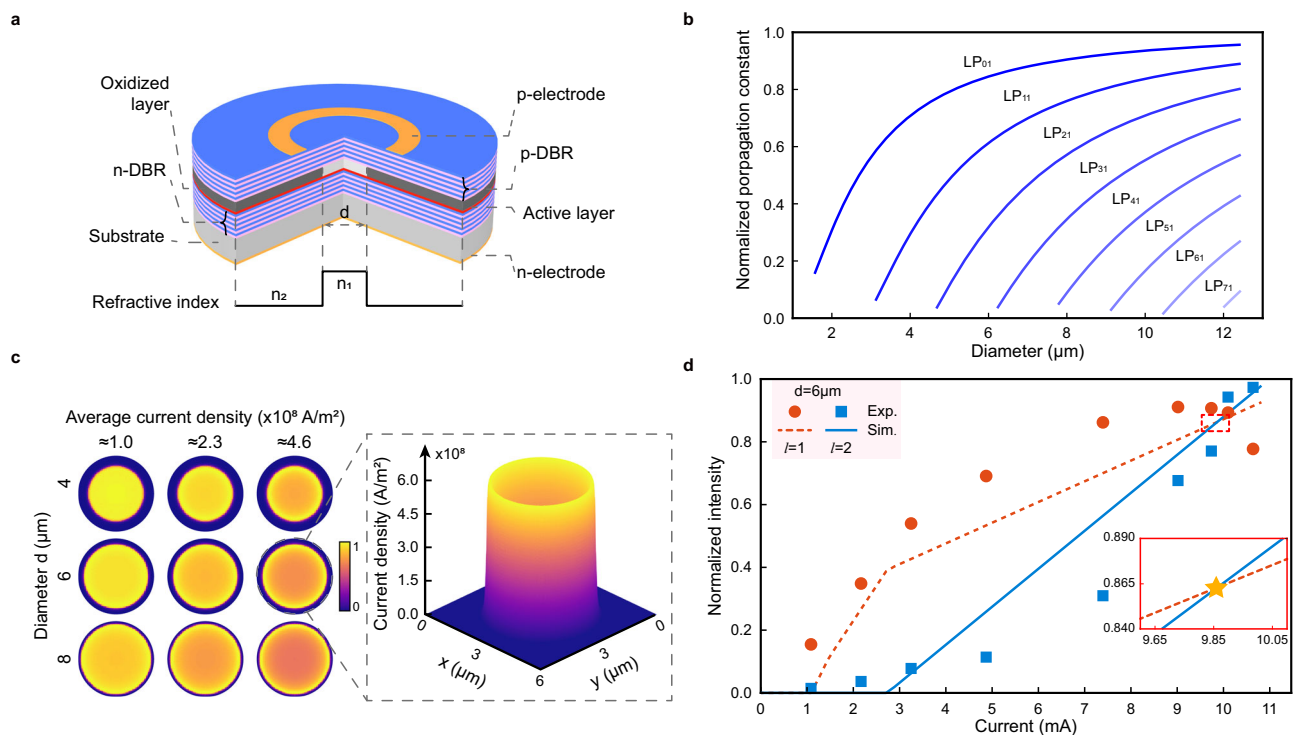


Fig. 2 | Injection current-dependent OAM modes dynamics in multimode VCSELs. **a** The detailed illustration of the VCSEL structure. **b** The OAM modes capacity of the multi-mode VCSELs with distinct oxide aperture diameters. **c** The emergency of spatial hole burning (SHB) effect at the active layer center of VCSEL

with the increase of the current and the oxide aperture size. **d** The theoretical and experimental observation of a dominant OAM mode component switching from $l=1$ to $l=2$ with the increase of injection current.

Gaussian profile at a low injection current for the VCSEL with a 4 μm -diameter oxide aperture, depleting carriers can be observed at the center with the increase of the current and the aperture size, which is termed the spatial hole burning (SHB) effect^{35,36}. The right inset of Fig. 2c illustrates a significant SHB phenomenon, which can be attributed to the preferential current flow along the annular edges of the VCSEL with a lower electrical resistance in accordance with Kirchhoff's law. Notably, the gains of each OAM mode are determined by continuously changing current densities, giving rise to the injection current-dependent OAM modes weighting coefficient spectra (Supplementary Note 2 and Supplementary Table 2). Simulating VCSELS with large oxide apertures is challenging due to increased computational complexity and potential modeling errors. In addition, devices with different aperture sizes are equivalent in revealing the principles of mode dynamics. Thus, without losing generality, we experimentally and theoretically investigated the weighting coefficients of OAM components with $l = 1$ and 2 for the VCSEL with a 6 μm -diameter oxide aperture (Fig. 2d). The theoretical results (the inset is the enlarged dashed box) suggests that the dominant OAM component switches from $l = 1$ to $l = 2$ at an injection current of ~ 10 mA, which is consistent with the experimental result.

Current-addressed mode-multiplexed holography

Implementing such current-dependent dominant OAM components for the design of an OAM-multiplexing hologram can enable current-addressed dynamic holographic displays. The schematic to measure the OAM mode components of the output electrical field provided by the VCSEL with a 30 μm -diameter oxide aperture is illustrated in Fig. 3a, wherein different spiral phase plates (SPPs) were adopted to achieve inverse OAM mode conversion ("Methods", Supplementary Fig. 4). As an example, the intensity distributions at the focal plane are given when the injection current is 28 mA, revealing the OAM modes weighting coefficient spectrum through the integrations of preset Gaussian profile areas (Fig. 3b). Notably, the OAM mode with $l = 25$ is a dominant component with the largest weighting coefficient. Next, the injection current was changed within the VCSEL's working range (Supplementary Fig. 5), leading to diverse weighting coefficient distributions of the eight OAM modes with $l = 22$ -29 (Fig. 3c). Supplementary Movie 1 directly visualizes the evolution of the light field under stepped current modulation, revealing the injection current-dependent spatial mode behavior of the VCSEL. To reduce the crosstalk in optical multiplexed holography, we elaborately propose an enumeration algorithm to identify distinct encoding OAM modes weighting coefficient spectra that feature a distinguishing largest weighting coefficient (Fig. 3d). The algorithm involves two main steps. First, the measured OAM weighting coefficients spectra are grouped, with each group containing four OAM mode components featuring distinct dominant OAM components. Second, the groups are evaluated to determine the one where the dominant OAM components show the greatest disparity in weighting coefficients compared to the other components within each spectrum. Hence, for the spatial modes obtained at four specific working currents ($I = 101, 67, 28,$ and 58 mA) (Supplementary Fig. 6), the OAM modes ($l = 23, 24, 25,$ and 26) have been regarded as the dominant OAM components in our scheme (Fig. 3c).

The design of the OAM-multiplexing hologram is illustrated in Fig. 4a (Supplementary Note 3). The Fourier holograms of four frames from a rotating windmill video are encoded by helical phase plates with OAM orders of $l = -25, -26, -24$ and -23 , then being superposed into the final OAM-multiplexing hologram. As a result, as the four selected injection currents ($I = 28, 58, 67,$ and 101 mA) switched at fixed time intervals, the target holographic images with an average peak signal-to-noise ratio (PSNR) exceeding 18.8 dB can be dynamically reconstructed by selectively recovering the Gaussian mode pixels (Fig. 4b). In comparison to the low-quality images reconstructed by beams

generated by the same VCSEL at the other randomly selected injection currents, the improvement of the average signal-to-noise ratio (SNR) suggests the effectiveness of the enumeration algorithm mentioned above (Supplementary Fig. 7). In addition, a spatial division scheme has been adopted in the design of the OAM-multiplexing hologram of a micro-quick response (MQR) code image, which leads to a current-shared holographic encryption. To construct the hologram, the MQR code image is divided into four sections, and sampled with a comb function (Fig. 4c). Then, the Fourier holograms are encoded with the selected helical phase plates ($l = -25, -26, -24,$ and -23), resulting in an OAM-multiplexing hologram. Therefore, after combining and binarizing the four reconstructive images obtained under the four selected injection currents, the complete MQR code image is obtained (Fig. 4d). Scanning the MQR code reveals the encrypted message "Hello World".

Ultra-compact holographic VCSEL chip with ultra-high frame rate

By directly printing OAM-multiplexing holograms onto the surface of the VCSEL (Methods, Supplementary Fig. 8), we successfully demonstrate a dynamic holographic VCSEL chip using the above-mentioned current-addressed modes multiplexing holography (Fig. 5). To experimentally characterize the performances of the chips, an on-chip measurement system has been developed (Fig. 5a), wherein the VCSEL chip was powered via a metal probe that directly contacted the p-electrode (inset in bottom right). When the currents were switched, independent holographic images can be observed in the charge-coupled device (CCD) camera (inset in upper right). In our scheme, four VCSELS with oxide aperture diameters of 8 μm , 10 μm , 12 μm , and 14 μm have been selected as the light sources to construct a device array (Fig. 5b and Supplementary Fig. 9). Considering the divergence angles of the VCSELS and the printed holder height (150 μm), the hologram size was set as 100 $\mu\text{m} \times 100 \mu\text{m}$ with a pixel size of 1 $\mu\text{m} \times 1 \mu\text{m}$ to ensure optimal illumination of each hologram (inset in bottom left). Notably, 8-level transmission-type phase modulation was adopted through controlling the height of each pixel pillar (inset in bottom right).

For holographic encoding in OAM multiplexing holography, two dominant OAM states at specific injection currents have been employed for each holographic VCSEL chip, respectively. Consequently, by switching the injection currents on each VCSEL (from 9 mA, 16 mA, 23 mA, 23 mA to 19 mA, 9 mA, 27 mA, 32 mA), the dynamic holographic display (from "HOLO" to "GRAM") can be obtained (Fig. 5c). Moreover, the current-addressed dynamic holographic display can be extended to 3D images by incorporating lens functions with varying focal lengths, thereby leveraging the depth information of the image along the light propagation direction (Supplementary Fig. 10). As such, when the holographic VCSEL chip was given as 10 mA or 18 mA, independent switchable images (Arabic number images "2, 0" or "0, 4") can be observed at separate image planes at a propagation distance of $z = 215 \mu\text{m}$ and $495 \mu\text{m}$ (Fig. 5d and Supplementary Fig. 11). Notably, the modulation response-frequency curve of the VCSEL chip illustrates that the refresh rate of the dynamic holographic display can reach up to ~ 1.93 GHz (Fig. 5e and Supplementary Fig. 12, "Methods"). We also conducted standard measurements of the frequency-dependent properties of the used VCSEL (Supplementary Figs. 13-15, Methods), which show that its bandwidth reaches up to 3 GHz. The gap between this bandwidth and the observed holographic refresh rate is mainly due to differences in the testing methods. These results indicate that further improvements in the packaging of the VCSEL holographic chip may support even higher refresh rates. Additionally, a diffraction grating hologram was printed onto the surface of the VCSEL to evaluate the diffraction efficiency of such an optical digitalized hologram. The diffraction efficiency is quantified

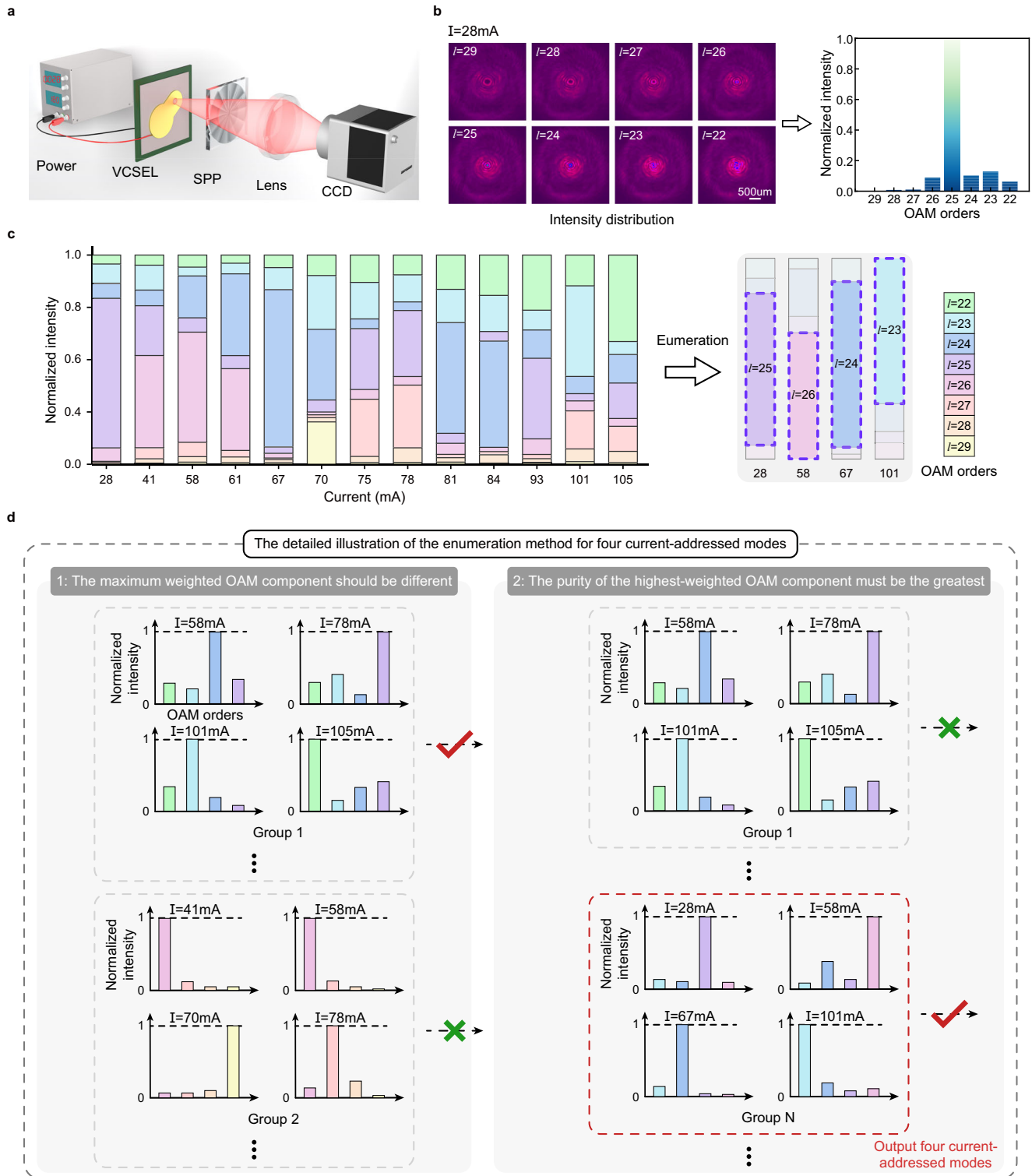


Fig. 3 | Principle of current-addressed mode-multiplexed holographic encoding. **a** Conceptual illustration of the optical setup. SPP: spiral phase plate. **b** The intensity distributions at the focal plane when VCSEL beams at an injection current of 28 mA illuminated on SPP with distinct OAM orders (left panel), the resultant OAM modes weighting coefficient spectra reveals that the OAM modes with $l = 25$ is a dominant component (right panel). **c** The OAM weighting coefficient distributions for various injection currents within the working range (left panel). Here, the pseudo-colors represent eight OAM modes with $l = 22-29$. After the enumeration algorithm, four encoding OAM modes that feature a distinguishing largest

weighting coefficient have been selected (right panel). **d** The detailed illustration of the enumeration algorithm for the four current-addressed modes. First, the measured OAM weighting coefficients spectra are grouped, with each group containing four OAM mode components featuring distinct dominant OAM components. Second, the groups are evaluated to determine the one where the dominant OAM components show the greatest disparity in weighting coefficients compared to the other components within each spectrum. As a result, the four dominant OAM components from the selected group can be utilized to design the OAM-multiplexing hologram.

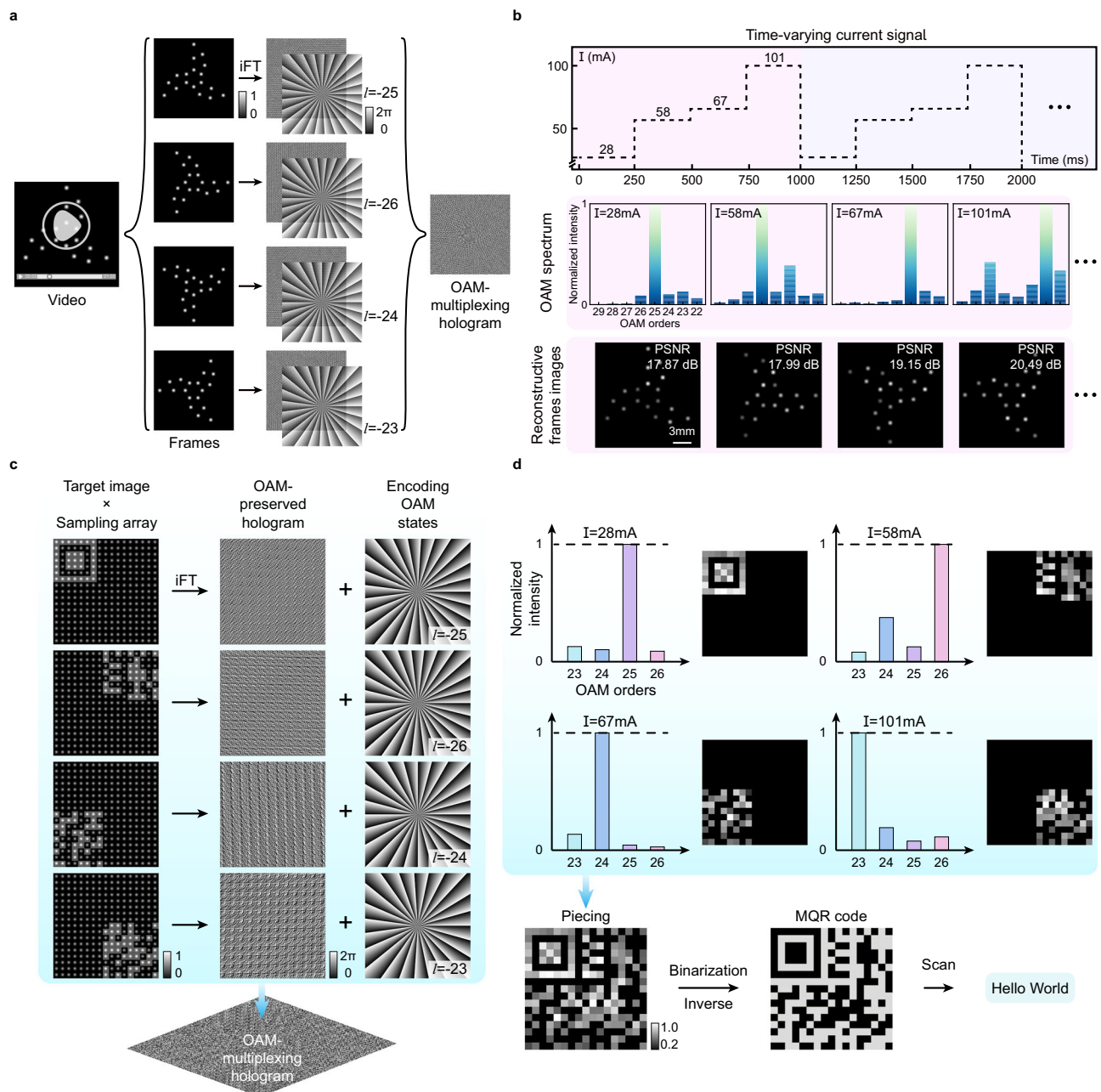


Fig. 4 | Current-addressed holographic video and current-shared holographic encryption scheme. **a** The design process of the OAM-multiplexing hologram for the target video comprising four image frames. **b** The reconstructive video images (bottom row), when switching the appropriate injection currents (middle row) at a time sequence of 250 ms (upper row). **c** Design process of the OAM-multiplexing

hologram of a MQR code image for current-shared holographic encryption. **d** Experimental reconstruction of the OAM-multiplexing hologram. After combining and binarizing the four reconstructive images, the complete MQR code image can be obtained. Scanning the MQR code reveals the encrypted message “Hello World”.

by the ratio of the intensity of the +1-order diffraction spot to the total output intensity of the VCSEL. The result indicates the final average modulation efficiency of 44.68%, which is determined by the grating diffraction efficiency and the transmission efficiency of the substrate (Supplementary Fig. 16).

Discussion

In summary, we develop a holographic VCSEL chip that eliminates the barriers to achieving an ultra-compact holographic system with dynamic light control capability. In this context, the injection current-dependent dominant OAM component states in multimode VCSELs are revealed to achieve current-addressed mode-multiplexed

holography. Through laser nanoprinting, OAM-multiplexing hologram (arrays) can be incorporated into the VCSELs, with each unit occupying merely hundreds of microns. A dynamic 3D holographic display is achieved by current-switching at frame rates up to ~1.93 GHz, enabled by the ultra-high modulation bandwidth of oxide-confined VCSEL architectures. Notably, VCSELs with larger oxide apertures support more spatial modes suitable for holographic encoding, thereby enhancing the multiplexing capacity (Supplementary Fig. S17). In addition, the principle of current-addressed mode-multiplexed holography can be applied in the design of metasurface holograms with subwavelength pixel resolution^{37,38}, where polarization-multiplexing strategies may be incorporated to further increase the available

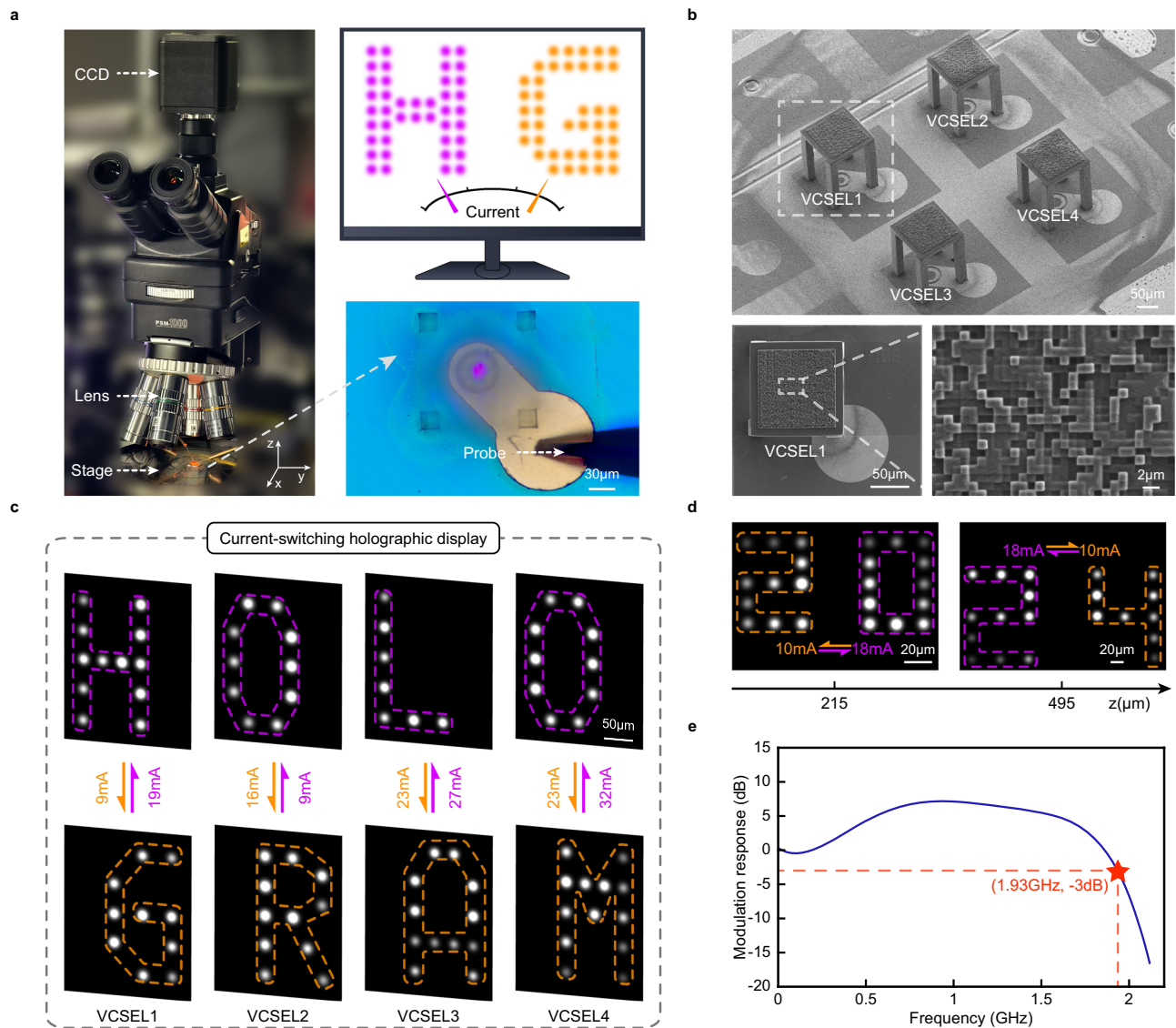


Fig. 5 | Ultra-compact holographic VCSEL chip with ultra-high frame rate.

a Photo of the on-chip measurement system to characterize the display performances (Left panel). The holographic VCSEL chip was powered via a metal probe that contacts the p-electrode (bottom right). The holographic images can be dynamically switched when changing the injection currents (upper right). **b** SEM

images of a holographic VCSEL chip comprising 2×2 hologram devices array.

c Current-switching holographic display. **d** Current-switching 3D holographic display at separate image planes. **e** The modulation response-frequency curve of the VCSEL chip, indicating a bandwidth of 1.93 GHz at -3 dB.

holographic channel numbers³⁹. Furthermore, VCSEL configurations, such as chaotic-cavity VCSELs^{40–42}, warrant further exploration. Their irregular geometries support a substantially larger number of transverse modes, theoretically enriching the available channels for multiplexed hologram design. However, chaotic-cavity VCSELs suffer from mode complexity and instability, which can degrade holographic performance and stability. Therefore, further co-design and optimization of the VCSEL structure and hologram algorithm may be required to address these challenges. It can be expected that the experimental realization of such an integrated, cost-effective and dynamic holographic system opens avenues for transformative applications in wearable devices⁴³, ultra-high-speed short-reach interconnects⁴⁴, virtual and augmented reality⁴⁵, and autonomous driving⁴⁶. This work bridges nanophotonics and optoelectronics, paving the way for next-generation dynamic holography in both scientific and industrial domains.

Methods

COMSOL multiphysics simulation

We used COMSOL Multiphysics 6.2 to calculate the current density distribution shown in Fig. 2c. First, we defined the global parameters, including both structural and material parameters, based on the epitaxial structure of the VCSELs (Supplementary Table 1). Using rotational symmetry modeling, we constructed the geometry of the VCSEL and assigned the appropriate materials to each region. The VCSEL diameter was set as the oxide aperture diameter plus $11 \mu\text{m}$, and the inner diameter of the annular p-contact was set as the oxide aperture diameter plus $3 \mu\text{m}$, following the device specifications. Next, we discretized the structure to enable an efficient and accurate solution of the physical field. A direct bandgap spontaneous emission light transition model was applied, and the steady-state equations were obtained through voltage sweeps and semiconductor equilibration. Finally, we analyzed the current distribution by examining a two-dimensional

cross-section, located 50 nm above the active region, under different voltage conditions.

Optical setup for the measurement of OAM components weighting spectra of VCSELs and the current-addressed holographic video

To measure the OAM components weighting spectra of VCSELs and obtain the current-addressed holographic video, the conceptual illustration and the practical optical setup can be found in Fig. 3a and Supplementary Fig. 4, respectively. The VCSEL operates under continuous-wave conditions. After supplying power on the VCSEL, a $\times 10$ objective lens was utilized to modulate the divergence angle of the light beams. Then, a half-wave plate in combination with a polarization beam splitter was employed to control the intensity of horizontal-polarized light beams continuously. After that, the beams illuminated on the spatial light modulator (SLM, model: PLUTO-NIR-010-A) and a CCD camera (model: Basler, acA2040-90uc) was put on the focal plane to capture the reconstructed holographic images. The OAM-multiplexing hologram in Fig. 4a and the helical phase plates with different OAM orders were imprinted on the SLM, respectively.

Laser nanoprinting of the holograms on the surfaces of the multimode VCSELs

A commercial photolithography system (Photonic Professional GT, Nanoscribe GmbH), equipped with a 780 nm, 80 MHz femtosecond laser, was used for printing. The process was conducted in a dip-in galvo-scan-mode configuration, utilizing the two-photon resist IP-Dip and a high numerical aperture objective lens (Plan-Apochromat 63x/1.40 Oil DIC, Zeiss). The printed structure consists of three key components: four supporting pillars ($20\ \mu\text{m} \times 20\ \mu\text{m} \times 140\ \mu\text{m}$ each), a supporting table ($120\ \mu\text{m} \times 120\ \mu\text{m} \times 10\ \mu\text{m}$), and the holographic plates ($100\ \mu\text{m} \times 100\ \mu\text{m}$).

The specific structural parameters are listed below. For the pillars, the slicing distance (step size in the longitudinal direction) was set to $0.5\ \mu\text{m}$, and the hatching distance (step size in the transverse direction) was set to $0.2\ \mu\text{m}$ to optimize printing speed. For the table, the slicing distance remained at $0.5\ \mu\text{m}$, but the hatching distance was reduced to $0.05\ \mu\text{m}$ to ensure a flat surface, as the laser beam must pass through it. The hologram height was $150\ \mu\text{m}$, and the slicing distance for the holograms was set to $0.226\ \mu\text{m}$, corresponding to a phase modulation of $\pi/4$ for the 905 nm VCSELs, with a hatching distance of $0.05\ \mu\text{m}$.

The detailed printing process is illustrated in Supplementary Fig. 8. The optimized printing parameters were as follows: 52 mW laser power and $20000\ \mu\text{m/s}$ scanning speed for the pillars, 46 mW and $20000\ \mu\text{m/s}$ for the table, and 40 mW and $10000\ \mu\text{m/s}$ for the holograms. After printing, the samples were developed by immersion in propylene glycol 1-monomethyl ether 2-acetate for 30 min, followed by rinsing in isopropanol for 5 min. The devices were then air-dried through evaporation.

Characterization of the holographic VCSEL chip

As shown in Supplementary Fig. 12, the frequency response of the VCSEL holographic chip was characterized using a vector network analyzer (Rohde & Schwarz ZNLE14). Here, VCSEL_2 in Fig. 5c was selected for testing and connected to the PCB via gold wire bonding, with external linkage to the driver power supply. First, harmonic modulation signals from the network analyzer were used to cyclically switch the injection current of VCSEL_2 between 9 mA and 16 mA, inducing periodic variations in the energy of each pixel featuring a Gaussian mode in the reconstructed 'O' pattern. Afterwards, the optical output from one pixel was coupled into a single-mode fiber and detected by a photodetector. The single-mode fiber ensured that the photodetector collected only the energy variations of the Gaussian mode within the pixel. Finally, the

photodetector output was analyzed using the network analyzer to obtain the modulation response–frequency curve.

In addition, the frequency-dependent characteristics of the used VCSELs were independently measured by a professional VCSEL manufacturer (Bixel Photonics Co., Ltd.). For these tests, the VCSELs were bonded onto a substrate, and the current signal was applied via SG probes. Modulation-response–frequency curves were acquired using the same procedure as in the holographic refresh-rate measurement, except that the photodetector directly collected the total optical output of the VCSELs. For the spectral-versus-frequency characterization, an arbitrary waveform generator (Anritsu MP1900A) replaced the vector network analyzer to provide high-speed modulation, and the resulting optical signal was coupled into an optical spectrum analyzer (YOKOGAWA AQ6370D) for spectral analysis.

The fundamental DC characteristics of the VCSELs used in our experiments, including I–V curves, emission spectra, and device lifetime, were also measured at Bixel Photonics Co., Ltd. Device lifetime was evaluated using a TO-LD drawer aging resistance testing system. Specifically, 29 VCSELs with $10\text{-}\mu\text{m}$ oxide aperture diameters were tested at an injection current of 16 mA and a temperature of $85\ ^\circ\text{C}$ for a total duration of 168 h. A typical failure criterion for VCSELs is defined as a 20% reduction in output power. All tested devices remained fully functional throughout the 168 h stress period, indicating a lifetime exceeding 168 h under accelerated conditions. Furthermore, assuming device operation at $50\ ^\circ\text{C}$ under a drive current of 16 mA, and employing the established activation energy ($E_a = -1.3\ \text{eV}$) reported in prior studies⁴⁷, together with the standard acceleration factor (AF) calculation model⁴⁸, we obtain an AF of 95.81 for the conditions of 16 mA at $85\ ^\circ\text{C}$ (aging) versus 16 mA at $50\ ^\circ\text{C}$ (usage). Accordingly, the estimated lifetime of the VCSELs under $50\ ^\circ\text{C}$ and 16 mA operating conditions exceeds 16,096 h.

Data availability

The main source data generated in this study have been deposited in the Figshare database under accession code <https://doi.org/10.6084/m9.figshare.31021633>.

Code availability

The code used for the hologram design is available from the corresponding author upon request.

References

1. Gabor, D. A new microscopic principle. *Nature* **161**, 777–778 (1948).
2. Tay, S. et al. An updatable holographic three-dimensional display. *Nature* **451**, 694–698 (2008).
3. Heanue, J. F., Bashaw, M. C. & Hesselink, L. Volume holographic storage and retrieval of digital data. *Science* **265**, 749–752 (1994).
4. Dang, S., Amin, O., Shihada, B. & Alouini, M.-S. What should 6G be? *Nat. Electron.* **3**, 20–29 (2020).
5. Qu, G. et al. Reprogrammable meta-hologram for optical encryption. *Nat. Commun.* **11**, 5484 (2020).
6. Lin, X. et al. All-optical machine learning using diffractive deep neural networks. *Science* **361**, 1004–1008 (2018).
7. Ha, S. T. et al. Optoelectronic metadevices. *Science* **386**, eadm7442 (2024).
8. Ding, F., Meng, C. & Bozhevolnyi, S. I. Electrically tunable optical metasurfaces. *Photonics Insights* **3**, R07 (2024).
9. Pan, G. et al. Harnessing the capabilities of VCSELs: unlocking the potential for advanced integrated photonic devices and systems. *Light Sci. Appl.* **13**, 229 (2024).
10. Huang, M. C. Y., Zhou, Y. & Chang-Hasnain, C. J. A surface-emitting laser incorporating a high-index-contrast subwavelength grating. *Nat. Photonics* **1**, 119–122 (2007).

11. Chen, Z. et al. Deep learning with coherent VCSEL neural networks. *Nat. Photonics* **17**, 723–730 (2023).
12. Zhang, C., Li, H. & Liang, D. Antireflective vertical-cavity surface-emitting laser for LiDAR. *Nat. Commun.* **15**, 1105 (2024).
13. Gu, M., Fang, X., Ren, H. & Goi, E. Optically digitalized holography: a perspective for all-optical machine learning. *Engineering* **5**, 363–365 (2019).
14. Xie, Y.-Y. et al. Metasurface-integrated vertical cavity surface-emitting lasers for programmable directional lasing emissions. *Nat. Nanotechnol.* **15**, 125–130 (2020).
15. Li, H. et al. Orbital angular momentum vertical-cavity surface-emitting lasers. *Optica* **2**, 547–552 (2015).
16. Dong, Y. et al. Nanoprinted diffractive layer integrated vertical-cavity surface-emitting vortex lasers with scalable topological charge. *Nano Lett.* **23**, 9096–9104 (2023).
17. Fu, P. et al. Metasurface enabled on-chip generation and manipulation of vector beams from vertical cavity surface-emitting lasers. *Adv. Mater.* **35**, 2204286 (2023).
18. Li, J. et al. Addressable metasurfaces for dynamic holography and optical information encryption. *Sci. Adv.* **4**, eaar6768 (2018).
19. Li, X. et al. Athermally photoreduced graphene oxides for three-dimensional holographic images. *Nat. Commun.* **6**, 6984 (2015).
20. Malek, S. C., Ee, H.-S. & Agarwal, R. Strain multiplexed metasurface holograms on a stretchable substrate. *Nano Lett.* **17**, 3641–3645 (2017).
21. Fan, Z. et al. Holographic multiplexing metasurface with twisted diffractive neural network. *Nat. Commun.* **15**, 9416 (2024).
22. Liu, X. et al. Thermally dependent dynamic meta-holography using a vanadium dioxide integrated metasurface. *Adv. Opt. Mater.* **7**, 1900175 (2019).
23. Li, X. et al. Multicolor 3D meta-holography by broadband plasmonic modulation. *Sci. Adv.* **2**, e1601102 (2016).
24. Xiong, B. et al. Breaking the limitation of polarization multiplexing in optical metasurfaces with engineered noise. *Science* **379**, 294–299 (2023).
25. Gao, H. et al. Dynamic 3D meta-holography in visible range with large frame number and high frame rate. *Sci. Adv.* **6**, eaba8595 (2020).
26. Zhang, Y., Zhu, S., Hu, J. & Gu, M. Femtosecond laser direct nanolithography of perovskite hydration for temporally programmable holograms. *Nat. Commun.* **15**, 6661 (2024).
27. Jin, L. et al. Dielectric multi-momentum meta-transformer in the visible. *Nat. Commun.* **10**, 4789 (2019).
28. Ren, H. et al. Complex-amplitude metasurface-based orbital angular momentum holography in momentum space. *Nat. Nanotechnol.* **15**, 948–955 (2020).
29. Rainer, M. Fundamentals, technology and applications of vertical-cavity surface-emitting lasers. *Springer Ser. Opt. Sci.* **166**, 560 (2013).
30. Fang, X., Ren, H. & Gu, M. Orbital angular momentum holography for high-security encryption. *Nat. Photonics* **14**, 102–108 (2020).
31. Wan, C. et al. Electric-driven meta-optic dynamics for simultaneous near-/far-field multiplexing display. *Adv. Funct. Mater.* **32**, 2110592 (2022).
32. Hadley, G. R. Effective index model for vertical-cavity surface-emitting lasers. *Opt. Lett.* **20**, 1483–1485 (1995).
33. Larsson, A. Advances in VCSELs for communication and sensing. *IEEE J. Sel. Top. Quantum Electron.* **17**, 1552–1567 (2011).
34. Zeng, X. et al. Experimental investigation of LP11 mode to OAM conversion in few mode-polarization maintaining fiber and the usage for all fiber OAM generator. *IEEE Photonics J.* **8**, 1–7 (2016).
35. Schatz, R. & Peeters, M. Modeling spatial hole burning and mode competition in index-guided VCSELs. *Proc. SPIE* **4942**, 158–169 (2002).
36. Wilson, G. C., Kuchta, D. M., Walker, J. D. & Smith, J. S. Spatial hole burning and self-focusing in vertical-cavity surface-emitting laser diodes. *Appl. Phys. Lett.* **64**, 542–544 (1994).
37. Yu, N. et al. Light propagation with phase discontinuities: generalized laws of reflection and refraction. *Science* **334**, 333–337 (2011).
38. Yang, H. et al. Angular momentum holography via a minimalist metasurface for optical nested encryption. *Light Sci. Appl.* **12**, 79 (2023).
39. Ni, P.-N. et al. Spin-decoupling of vertical cavity surface-emitting lasers with complete phase modulation using on-chip integrated jones matrix metasurfaces. *Nat. Commun.* **13**, 7795 (2022).
40. Lu, H., Alkhazragi, O., Lin, H., Ng, T. K. & Ooi, B. S. Shaping the light of VCSELs through cavity geometry design. *Light Sci. Appl.* **14**, 344 (2025).
41. Ma, C.-G., Xiao, J.-L., Xiao, Z.-X., Yang, Y.-D. & Huang, Y.-Z. Chaotic microlasers caused by internal mode interaction for random number generation. *Light Sci. Appl.* **11**, 187 (2022).
42. Sciamanna, M. & Shore, K. A. Physics and applications of laser diode chaos. *Nat. Photonics* **9**, 151–162 (2015).
43. Li, C. et al. Wearable and biocompatible blood oxygen sensor based on heterogeneously integrated lasers on a laser-induced graphene electrode. *ACS Appl. Electron.* **4**, 1583–1591 (2022).
44. Cui, Y. et al. Single-mode chirped high-contrast metastructure VCSEL for 106 Gbps PAM4 transmission. *Optica* **11**, 1567–1574 (2024).
45. Chang, C., Bang, K., Wetzstein, G., Lee, B. & Gao, L. Toward the next-generation VR/AR optics: a review of holographic near-eye displays from a human-centric perspective. *Optica* **7**, 1563–1578 (2020).
46. Skirnewskaja, J. & Wilkinson, T. D. Automotive holographic head-up displays. *Adv. Mater.* **34**, 2110463 (2022).
47. Ledentsov, N. N. et al. VCSELs: Influence of Design on Performance and Data Transmission over Multi-Mode and Single-Mode Fibers. *Photonics* **12**, 1037 (2025).
48. Herrick, R. W. Reliability of vertical-cavity surface-emitting lasers. *Jpn. J. Appl. Phys.* **51**, 11PC01 (2012).

Acknowledgements

We acknowledge the funding support from the National Natural Science Foundation of China (62422509, X.F., 62575180, B.L.), the Shanghai Natural Science Foundation (23ZR1443700, X.F., 25ZR1402386, B.L.), the Shanghai Science and Technology Innovation Action Plan (25LN3201000, X.F.), the Shuguang Program of Shanghai Education Development Foundation and Shanghai Municipal Education Commission (23SG41, X.F.), the Young Elite Scientist Sponsorship Program by CAST (No. 20220042, X.F.), the Shanghai Municipal Science and Technology Major Project (M.G.), the Shanghai Frontiers Science Center Program (2021–2025 No. 20, M.G.), and the Shanghai Sailing Program (23YF1429500, Y.D.). We also thank Mr. Ke Cheng for his assistance with graphic illustrations.

Author contributions

X.F. proposed the idea and conceived the experiment. M.G. and X.F. supervised the project. X.H., Y.D., and X.F. constructed the experiment and acquired the data. X.H., Y.D., J.S., B.L., H.L., N.C., M.G., and X.F. analyzed the results. X.F. and M.G. completed the writing of the paper with the contributions of all authors. Correspondence and requests for materials should be addressed to M.G. or X.F.

Competing interests

The authors declare no competing interests.

Additional information

Supplementary information The online version contains supplementary material available at <https://doi.org/10.1038/s41467-026-68938-8>.

Correspondence and requests for materials should be addressed to Min Gu or Xinyuan Fang.

Peer review information *Nature Communications* thanks Omar Alkhazragi and the other anonymous reviewer(s) for their contribution to the peer review of this work. A peer review file is available.

Reprints and permissions information is available at <http://www.nature.com/reprints>

Publisher's note Springer Nature remains neutral with regard to jurisdictional claims in published maps and institutional affiliations.

Open Access This article is licensed under a Creative Commons Attribution-NonCommercial-NoDerivatives 4.0 International License, which permits any non-commercial use, sharing, distribution and reproduction in any medium or format, as long as you give appropriate credit to the original author(s) and the source, provide a link to the Creative Commons licence, and indicate if you modified the licensed material. You do not have permission under this licence to share adapted material derived from this article or parts of it. The images or other third party material in this article are included in the article's Creative Commons licence, unless indicated otherwise in a credit line to the material. If material is not included in the article's Creative Commons licence and your intended use is not permitted by statutory regulation or exceeds the permitted use, you will need to obtain permission directly from the copyright holder. To view a copy of this licence, visit <http://creativecommons.org/licenses/by-nc-nd/4.0/>.

© The Author(s) 2026